(article starts on next page)

Edge rotation from momentum transport by neutrals

To cite this article: JT Omotani *et al* 2016 *J. Phys.: Conf. Ser.* **775** 012011

View the article online for updates and enhancements.

Edge rotation from momentum transport by neutrals

JT Omotani[1], SL Newton[1,2], I Pusztai[1] and T Fülöp[1]

[1]Department of Physics, Chalmers University of Technology, 41296 Gothenburg, Sweden
[2]CCFE, Culham Science Centre, Abingdon, Oxon, OX14 3DB, UK

E-mail: `omotani@chalmers.se`

Abstract. Due to their high cross field mobility, neutral atoms can have a strong effect on transport even at the low relative densities found inside the separatrix. We use a charge-exchange dominated model for the neutrals, coupled to neoclassical ions, to calculate momentum transport when it is dominated by the neutrals. We can then calculate self-consistently the radial electric field and predict the intrinsic rotation in an otherwise torque-free plasma. Using a numerical solver for the ion distribution to allow arbitrary collisionality, we investigate the effects of inverse aspect ratio and elongation on plasma rotation. We also calculate the rotation of a trace carbon impurity, to facilitate future comparison to experiments using charge exchange recombination spectroscopy diagnostics.

1. Introduction

Tokamak plasmas typically rotate, even in the absence of external momentum input. Rotation is crucial to performance since it stabilizes magnetohydrodynamic instabilities such as the resistive wall mode [1] and flow shear suppresses turbulence in the pedestal, leading to the high-confinement mode (H-mode) [2]. Intrinsic rotation is particularly important for future tokamaks such as ITER because the torque from NBI heating will be weaker in larger devices. Neutral particles, which are always present in the edge of the confined plasma volume, provide a mechanism to generate intrinsic rotation. They may give large momentum transport even at low relative density due to their high cross field mobility, as has been demonstrated theoretically [3–11]. The importance of neutrals for the edge plasma is confirmed by experimental evidence of the influence of neutral density and location on H-mode confinement and the low to high confinement transition threshold [12–22]. The neutrals may be localized poloidally due to gas fuelling at a particular location, or divertor recycling causing the neutrals to be concentrated near the X-point. The resulting momentum transport and rotation is then controlled by the location of the neutrals [10, 11, 23]. In Ref. [23] we presented a numerical framework with which the rotation can be calculated for such scenarios, allowing for arbitrary plasma collisionality. In this paper we validate our numerical procedure against the analytical limits given in Refs. [10, 11] for asymptotic collisionality regimes. We investigate the effects of the lowest order equilibrium shaping parameters (i.e. those with the smallest poloidal mode numbers), inverse aspect ratio ϵ and elongation κ. Finally, we consider impurity rotation. Plasma rotation is usually determined by charge exchange recombination spectroscopy [24] which often measures the rotation of an impurity species. The main ion and impurity rotation are known to differ [25]. We demonstrate that by including a trace impurity species in our simulations, both the bulk ion and the impurity rotation can be calculated within our framework for arbitrary collisionality of either species.

2. Momentum transport by neutrals

2.1. Model

The evolution of the radial electric field E_r in a tokamak plasma is determined by the radial current through Ampère's law. In steady state the radial current must vanish. The radial particle fluxes $\boldsymbol{\Gamma}_a$ of the charged species are then determined by the toroidal component of the momentum equations for species a [26],

$$\langle e_a \boldsymbol{\Gamma}_a \cdot \nabla\psi \rangle = \left\langle R\hat{\boldsymbol{\zeta}} \cdot \nabla \cdot \boldsymbol{\pi}_a \right\rangle - \langle RF_{a\zeta} \rangle - \left\langle n_a e_a R E_\zeta^{(A)} \right\rangle \tag{1}$$

for ions, electrons or neutrals. Here $\langle ... \rangle$ denotes the flux surface average, $2\pi\psi$ is the poloidal flux, R is the major radius, $\hat{\boldsymbol{\zeta}} = \nabla\zeta/|\nabla\zeta|$ is the unit vector in the direction of the toroidal angle ζ, $\boldsymbol{E}^{(A)}$ is the induced electric field and for the species a, e_a is the charge, $\boldsymbol{\pi}_a$ the viscosity tensor and $\boldsymbol{F}_a = \sum_b \boldsymbol{F}_{ab}$ the total friction force due to collisions with all other species b. $E_\zeta^{(A)}$ does not contribute to the radial current due to quasineutrality and $\sum_a \boldsymbol{F}_a = 0$ as momentum is conserved in collisions. For charged particles the viscosity component in (1) is typically negligible [26], leading to automatic ambipolarity at lowest order in the gyroradius expansion of standard neoclassical theory for a fully ionized plasma, so the radial electric field $E_r = -|\nabla\psi|\,\partial\Phi_0/\partial\psi$ is not constrained at this order [27–29]. However, neutrals have a non-negligible viscosity due to their high radial mobility which, as has been shown in the previous analytical work and is outlined below, depends on the toroidal velocity directly and therefore can constrain the electric field.

Since $\nabla(R\hat{\boldsymbol{\zeta}})$ is an antisymmetric tensor, while $\boldsymbol{\pi}_a$ is symmetric, then in the absence of external torques the vanishing of the radial current in steady state, where the sum on species a is over ions, electrons and neutrals, implies

$$0 = j_r = \sum_a \langle e_a \boldsymbol{\Gamma}_a \cdot \nabla\psi \rangle \approx \left\langle \nabla \cdot \left(R\hat{\boldsymbol{\zeta}} \cdot \boldsymbol{\pi}_{\mathrm{n}} \right) \right\rangle = \frac{1}{V'}\frac{d}{d\psi}\left(V' \left\langle R\hat{\boldsymbol{\zeta}} \cdot \boldsymbol{\pi}_{\mathrm{n}} \cdot \nabla\psi \right\rangle \right)$$

$$\Rightarrow \left\langle R\hat{\boldsymbol{\zeta}} \cdot \boldsymbol{\pi}_{\mathrm{n}} \cdot \nabla\psi \right\rangle = 0, \tag{2}$$

with $V' = \oint d\theta\,(\boldsymbol{B}\cdot\nabla\theta)^{-1}$, and we have noted that in the absence of external torque the boundary condition in the interior of the plasma is that the radial flux of toroidal angular momentum vanishes.

To compute the viscosity $\boldsymbol{\pi}_{\mathrm{n}}$ of the neutrals (denoted by subscript n) we solve the steady state neutral kinetic equation [6], assuming charge exchange (CX) dominates so that we may neglect other atomic processes,

$$\boldsymbol{v} \cdot \nabla f_{\mathrm{n}} = \frac{1}{\tau_{\mathrm{CX}}}\left(\frac{n_{\mathrm{n}}}{n_{\mathrm{i}}} f_{\mathrm{i}} - f_{\mathrm{n}} \right), \tag{3}$$

where f_a and n_a are the distribution function and density of a species a (we denote the bulk ions by subscript i). The CX collision frequency is $\tau_{\mathrm{CX}}^{-1} = n_{\mathrm{i}} \langle \sigma v \rangle_{\mathrm{CX}} \simeq 2.93 n_{\mathrm{i}} \sigma_{\mathrm{CX}} (T_{\mathrm{i}}/m_{\mathrm{i}})^{1/2}$ [6], which is larger than the ionization or recombination rates for tokamak edge parameters [30]; the CX rate is $\sim 40\%$ larger than the ionization rate at the 300 eV temperature we consider below, while recombination is negligible above a few eV [31]. Since we assume that the neutrals are dominated by charge exchange collisions with the ions, their temperature is the same as the ion temperature to lowest order, as the solution below shows. $\langle \sigma v \rangle_{\mathrm{CX}}$ is the thermal charge exchange rate coefficient and σ_{CX} is the charge exchange cross section for thermal particles. We will assume that the relative neutral density $n_{\mathrm{n}}/n_{\mathrm{i}}$ is small enough that the ion distribution is not affected directly by the neutrals, i.e. f_{i} is independent of f_{n}. We can then solve (3) with a

short mean-free-path expansion $f_{\mathrm{n}} = f_{\mathrm{n}}^{(0)} + f_{\mathrm{n}}^{(1)} + ...$ in $\tau_{\mathrm{CX}} v_{\mathrm{T}}/L \ll 1$, where $v_{\mathrm{T}} = \sqrt{2T_{\mathrm{i}}/m_{\mathrm{i}}}$ is the thermal velocity, with the ion temperature T_{i} and mass m_{i}, and L is a typical length scale of plasma parameters, giving

$$f_{\mathrm{n}}^{(0)} = \frac{n_{\mathrm{n}}}{n_{\mathrm{i}}} f_{\mathrm{i}}; \quad f_{\mathrm{n}}^{(1)} = -\tau_{\mathrm{CX}} \boldsymbol{v} \cdot \nabla f_{\mathrm{n}}^{(0)} = -\tau_{\mathrm{CX}} \boldsymbol{v} \cdot \nabla \left(\frac{n_{\mathrm{n}}}{n_{\mathrm{i}}} f_{\mathrm{i}} \right). \tag{4}$$

The neutral viscosity is then

$$\boldsymbol{\pi}_{\mathrm{n}} = m_{\mathrm{i}} \int d^3 v \left(\boldsymbol{vv} - \frac{1}{3} v^2 \mathbb{I} \right) f_{\mathrm{n}} = \frac{n_{\mathrm{n}}}{n_{\mathrm{i}}} \boldsymbol{\pi}_{\mathrm{i}} - \tau_{\mathrm{CX}} m_{\mathrm{i}} \int d^3 v \left(\boldsymbol{vv} - \frac{1}{3} v^2 \mathbb{I} \right) \boldsymbol{v} \cdot \nabla \left(\frac{n_{\mathrm{n}}}{n_{\mathrm{i}}} f_{\mathrm{i}} \right). \tag{5}$$

The first term can be neglected as the off-diagonal components of $\boldsymbol{\pi}_{\mathrm{i}}$ are small, leaving

$$R\hat{\boldsymbol{\zeta}} \cdot \boldsymbol{\pi}_{\mathrm{n}} \cdot \nabla \psi \approx -R\tau_{\mathrm{CX}} m_{\mathrm{i}} \int d^3 v \left(\hat{\boldsymbol{\zeta}} \cdot \boldsymbol{v} \right) (\nabla \psi \cdot \boldsymbol{v}) \, \boldsymbol{v} \cdot \nabla \left(\frac{n_{\mathrm{n}}}{n_{\mathrm{i}}} f_{\mathrm{i}} \right)$$

$$\approx -\frac{R\tau_{\mathrm{CX}} m_{\mathrm{i}}}{n_{\mathrm{i}}} \frac{dn_{\mathrm{n}}}{d\psi} \int d^3 v \left(\hat{\boldsymbol{\zeta}} \cdot \boldsymbol{v} \right) (\nabla \psi \cdot \boldsymbol{v})^2 f_{\mathrm{i}}, \tag{6}$$

assuming that the radial gradient of n_{n} dominates over those of the background plasma profiles and over any poloidal gradients.

Accounting for the gyroradius correction, the ion distribution function at the particle position $\boldsymbol{r}$ is

$$f_{\mathrm{i}}(\boldsymbol{r}) \approx f_{\mathrm{i,gc0}}(\boldsymbol{r}) - \frac{e\Phi_1}{T_{\mathrm{i}}} f_{\mathrm{i,gc0}}(\boldsymbol{r}) - \boldsymbol{\rho} \cdot \nabla f_{\mathrm{i,gc0}}(\boldsymbol{r}) + g_{\mathrm{i}}(\boldsymbol{r}), \tag{7}$$

where $f_{\mathrm{i,gc0}}$ is a Maxwellian, $\boldsymbol{\rho} = \boldsymbol{r} - \boldsymbol{R}_{\mathrm{gc}}$ is the gyroradius vector with $\boldsymbol{R}_{\mathrm{gc}}$ the guiding centre position, $\Phi_1 = \Phi - \langle \Phi \rangle$ is the poloidally varying part of the electrostatic potential Φ and 0, 1 subscripts refer to the order in a $\delta = \rho/L$ gyroradius expansion. We will obtain the non-adiabatic part of the perturbed distribution function, $g_{\mathrm{i}} = f_{\mathrm{i,gc1}} + \frac{e_{\mathrm{i}}\Phi_1}{T_{\mathrm{i}}} f_{\mathrm{i,gc0}}$, from numerical solutions of the first order drift kinetic equation. The first two terms on the right of (7) are isotropic in velocity, so do not contribute to (6), and we have

$$R\hat{\boldsymbol{\zeta}} \cdot \boldsymbol{\pi}_{\mathrm{n}} \cdot \nabla \psi \approx \left(R\hat{\boldsymbol{\zeta}} \cdot \boldsymbol{\pi}_{\mathrm{n}} \cdot \nabla \psi \right)^{(\mathrm{dia})} + \left(R\hat{\boldsymbol{\zeta}} \cdot \boldsymbol{\pi}_{\mathrm{n}} \cdot \nabla \psi \right)^{(\mathrm{neo})}, \tag{8}$$

where

$$\left(R\hat{\boldsymbol{\zeta}} \cdot \boldsymbol{\pi}_{\mathrm{n}} \cdot \nabla \psi \right)^{(\mathrm{dia})} = \frac{\tau_{\mathrm{CX}} R^4 B_{\mathrm{p}}^4 T_{\mathrm{i}}^2}{e B^2} \frac{dn_{\mathrm{n}}}{d\psi} \left(\frac{d \ln p_{\mathrm{i}}}{d\psi} + \frac{e}{T_{\mathrm{i}}} \frac{d\Phi_0}{d\psi} + \frac{d \ln T_{\mathrm{i}}}{d\psi} \right) \tag{9}$$

$$\left(R\hat{\boldsymbol{\zeta}} \cdot \boldsymbol{\pi}_{\mathrm{n}} \cdot \nabla \psi \right)^{(\mathrm{neo})} = -\frac{\tau_{\mathrm{CX}} R^2 B_{\mathrm{p}}^2 I m_{\mathrm{i}}}{2 B n_{\mathrm{i}}} \frac{dn_{\mathrm{n}}}{d\psi} \int d^3 v \, v_\parallel v_\perp^2 g_{\mathrm{i}}, \tag{10}$$

with B_{p} the poloidal magnetic field strength, $I = R\boldsymbol{B} \cdot \hat{\boldsymbol{\zeta}}$ and parallel and perpendicular taken relative to the background magnetic field. Drift velocity terms do not appear in (10) as they are second order in δ. This momentum flux is first order in δ, and therefore large compared to that of the ions, as the neutral distribution $f_{\mathrm{n}}^{(1)}$ is strongly anisotropic in gyroangle.

2.2. Interpretation

It is useful to write the momentum flux (8) in terms of the toroidal velocity and heat flux in order to explain the physical origins of the intrinsic momentum flux. This is done as follows. We can write (9) in terms of the toroidal components of the diamagnetic flow and heat flux [11]

$$V_\zeta^{(\mathrm{dia})} = -\frac{RB_\mathrm{p}^2 T_\mathrm{i}}{eB^2}\left(\frac{d\ln p_\mathrm{i}}{d\psi} + \frac{e}{T_\mathrm{i}}\frac{d\Phi_0}{d\psi}\right); \quad \frac{2q_\zeta^{(\mathrm{dia})}}{5p_\mathrm{i}} = -\frac{RB_\mathrm{p}^2 T_\mathrm{i}}{eB^2}\frac{d\ln T_\mathrm{i}}{d\psi}, \tag{11}$$

as

$$\left(R\hat{\boldsymbol{\zeta}}\cdot\boldsymbol{\pi}_\mathrm{n}\cdot\nabla\psi\right)^{(\mathrm{dia})} = -\tau_\mathrm{CX}R^3 B_\mathrm{p}^2 T_\mathrm{i}\frac{dn_\mathrm{n}}{d\psi}\left(V_\zeta^{(\mathrm{dia})} + \frac{2q_\zeta^{(\mathrm{dia})}}{5p_\mathrm{i}}\right). \tag{12}$$

To rewrite (10) note that $v_\parallel v_\perp^2 = \frac{2}{5}v_\parallel v^2 - \frac{2}{5}v^3 P_3(\xi)$ where $\xi = v_\parallel/v$ is the cosine of the pitch angle and $P_3(\xi) \equiv 5\xi^3/2 - 3\xi/2$ is the third order Legendre polynomial. The neoclassical part of the total heat flux is

$$\frac{I}{RB}\int d^3v\,\frac{m_\mathrm{i}}{2}v_\parallel v^2 g_\mathrm{i} \equiv \frac{I}{RB}Q_{\mathrm{i}\parallel}^{(\mathrm{neo})} \approx Q_{\mathrm{i}\zeta}^{(\mathrm{neo})} = q_{\mathrm{i}\zeta}^{(\mathrm{neo})} + \frac{5p_\mathrm{i}}{2}V_{\mathrm{i}\zeta}^{(\mathrm{neo})} + \mathcal{O}(\delta^3) \tag{13}$$

and so (10) gives

$$\left(R\hat{\boldsymbol{\zeta}}\cdot\boldsymbol{\pi}_\mathrm{n}\cdot\nabla\psi\right)^{(\mathrm{neo})} \approx -\tau_\mathrm{CX}R^3 B_\mathrm{p}^2 T_\mathrm{i}\frac{dn_\mathrm{n}}{d\psi}\left(V_{\mathrm{i}\zeta}^{(\mathrm{neo})} + \frac{2}{5p_\mathrm{i}}q_{\mathrm{i}\zeta}^{(\mathrm{neo})}\right) + \frac{\tau_\mathrm{CX}R^2 B_\mathrm{p}^2 Im_\mathrm{i}}{5Bn_\mathrm{i}}\frac{dn_\mathrm{n}}{d\psi}\int d^3v\,v^3 P_3(\xi)g_\mathrm{i}. \tag{14}$$

Thus we have finally

$$\left(R\hat{\boldsymbol{\zeta}}\cdot\boldsymbol{\pi}_\mathrm{n}\cdot\nabla\psi\right) \approx -\tau_\mathrm{CX}R^3 B_\mathrm{p}^2 T_\mathrm{i}\frac{dn_\mathrm{n}}{d\psi}\left(V_{\mathrm{i}\zeta} + \frac{2}{5p_\mathrm{i}}q_{\mathrm{i}\zeta}\right) + \frac{\tau_\mathrm{CX}R^2 B_\mathrm{p}^2 Im_\mathrm{i}}{5Bn_\mathrm{i}}\frac{dn_\mathrm{n}}{d\psi}\int d^3v\,v^3 P_3(\xi)g_\mathrm{i} \tag{15}$$

and we see that the steady state condition (2) is largely set by a balance between the toroidal friction and heat friction, with an additional contribution from the third Legendre component of the distribution function.[1]

The plasma flow and heat flux take the general form [26]

$$\boldsymbol{V}_\mathrm{i} = -\left(\frac{d\Phi_0}{d\psi} + \frac{1}{en_\mathrm{i}}\frac{dp_\mathrm{i}}{d\psi}\right)R\hat{\boldsymbol{\zeta}} - \frac{kI}{e\langle B^2\rangle}\frac{dT_\mathrm{i}}{d\psi}\boldsymbol{B} \tag{16}$$

$$\boldsymbol{q}_\mathrm{i} = -\frac{5p_\mathrm{i}}{2e}\frac{dT_\mathrm{i}}{d\psi}R\hat{\boldsymbol{\zeta}} + \frac{5lIp_\mathrm{i}}{2e\langle B^2\rangle}\frac{dT_\mathrm{i}}{d\psi}\boldsymbol{B}, \tag{17}$$

where k and l are dimensionless parameters that depend on the plasma collisionality. k varies from positive in the Pfirsch-Schlüter regime, (21), to negative in the banana regime, (24), while l remains positive, with $l = 1$ in the Pfirsch-Schlüter regime and slightly smaller in the banana regime, (24).

The neutral source is often poloidally localized, for example from a gas-puff valve or divertor recycling. Modelling the neutral density as a δ-function at $\theta = \theta_\mathrm{n}$, the flux surface average in (2) simply evaluates its argument at the poloidal location θ_n. Neglecting here, for illustrative

---

[1] Note that this form is evaluated for arbitrary bulk ion collisionality. The g_i appearing here corresponds to the usual $F + g^{\mathrm{banana}}$ in the low collisionality regime, giving rise to the equivalent expression (17) in Ref. [11].

purposes, the P_3 term we can use (15) in (2) to solve for the electric field, and hence also the rotation, as

$$-\frac{d\Phi_0}{d\psi} \approx \frac{T_i}{en_i}\frac{dn_i}{d\psi} + \frac{1}{e}\left(2 + \frac{(k-l)I^2}{R_n^2\langle B^2\rangle}\right)\frac{dT_i}{d\psi}; \quad V_{i\zeta} \approx \left(R + \frac{(k-l)I^2 R}{R_n^2\langle B^2\rangle} - \frac{kI^2}{R\langle B^2\rangle}\right)\frac{1}{e}\frac{dT_i}{d\psi}, \quad (18)$$

where $R_n = R(\theta_n)$ is the major radius at which the neutrals are located. Thus the sign of $(k-l)$ determines the sign of the variation of E_r with R_n. At high collisionality $(k-l) < 0$ so E_r is more negative for small R_n, while at low collisionality $(k-l) > 0$ so E_r is more positive for small R_n. An accurate analytic form in the banana regime was given in Ref. [11], (22) here; it has the same $(k-l)$ prefactor for its R_n dependence, indicating that the preceding discussion does capture the origin of the trends. The toroidal velocity has a similar variation with R_n as it comes from substituting $d\Phi_0/d\psi$ into (16). These features can be identified in the numerical results shown in the following section.

3. Simulation results

As can be seen from Eq. (10) we need the ion guiding centre distribution function to determine the steady state radial electric field and toroidal flow. To calculate this we use the Pedestal and Edge Radially-global Fokker-Planck Evaluation of Collisional Transport (PERFECT) neoclassical solver [32], used here as a radially-local solver. Taking a guess for $d\Phi_0/d\psi$ we use the distribution function from PERFECT to calculate the neutral momentum flux, and iterate on $d\Phi_0/d\psi$ to find the value consistent with the steady state condition, Eq. 2. While experimental equilibria can be used, here we take model divertor magnetic geometries based on analytical solutions to the Grad-Shafranov equation [33], allowing trends in the rotation behaviour with shaping parameters to be identified. The geometry is parameterized in terms of the inverse aspect ratio ϵ, elongation κ and triangularity δ, as well as the major radius R_X and height Z_X of the X-point, along with the toroidal $\beta_t = 2\mu_0\bar{p}/B_0^2$ (where $\bar{p}$ is the volume averaged pressure) and plasma current. Dimensional scales are set by the major radius of the plasma centre R_0 and the vacuum magnetic field at the centre B_0. We take the nominal scan parameters representative of ITER [33]: $R_0 = 6.2$ m, $B_0 = 5.3$ T, $\epsilon = 0.32$, $\kappa = 1.7$, $\delta = 0.33$, $R_X = (1 - 1.1\delta\epsilon)R_0$, $Z_X = -1.1\kappa\epsilon R_0$ and $\beta_t = 0.05$. We allow the plasma current to vary to keep the safety factor q_{95} of the flux surface with normalized poloidal flux $\psi_N = 0.95$ fixed to the value 2.84, corresponding to a plasma current of 15 MA in the baseline equilibrium. The neutrals are poloidally localized, represented by a delta function[2] in poloidal angle $n_n = \hat{n}_n(\psi)\delta(\theta - \theta_n)$, on the $\psi_N = 0.95$ flux surface. The main ion species and neutrals are both deuterium and we do not need to solve the electron kinetic equation here due to the small mass ratio.

Below we show scans plotted at fixed collisionality. We use the collisionality $\hat{\nu} = \nu_{ii}L_\parallel/v_T$, with ν_{ii} the ion-ion collision frequency, calculated using the connection length $L_\parallel = \int_{\theta=0}^{\theta=2\pi} dl_\parallel/2\pi$, where $dl_\parallel$ is the line element parallel to $\boldsymbol{B}$, which reduces to $L_\parallel \approx qR_0$ in the large aspect ratio limit. The baseline value is $\nu_{ii}L_\parallel/v_T \approx 1.26$ corresponding to $T_i = 300$ eV and $n_i = 10^{20}$ m^{-3} in the baseline equilibrium. We set the collisionality by varying the density at fixed temperature and logarithmic temperature gradient. To give explicit rotation velocities and electric fields in physical units, we choose a scale length for the ion temperature gradient, at the outboard midplane, of $L_{Ti} = 10$ cm in the baseline equilibrium. In section 3.2 where we scan the equilibrium geometry, we hold fixed the gradient in poloidal flux at the value $\partial \ln T_i/\partial\psi = -1/L_{Ti}|\nabla\psi| \approx 0.911$ T^{-1} m^{-2} corresponding to $L_{Ti} = 10$ cm in the baseline equilibrium. We set $\partial n_i/\partial\psi = 0$ here. The density gradient $\partial n_i/\partial\psi$ and electrostatic potential

---

[2] The delta function representation takes the poloidal width of the neutral density variation to be narrow compared to the minor radius, but the poloidal width should be understood to be large compared to the radial gradient scale length, so that poloidal derivatives may be neglected.
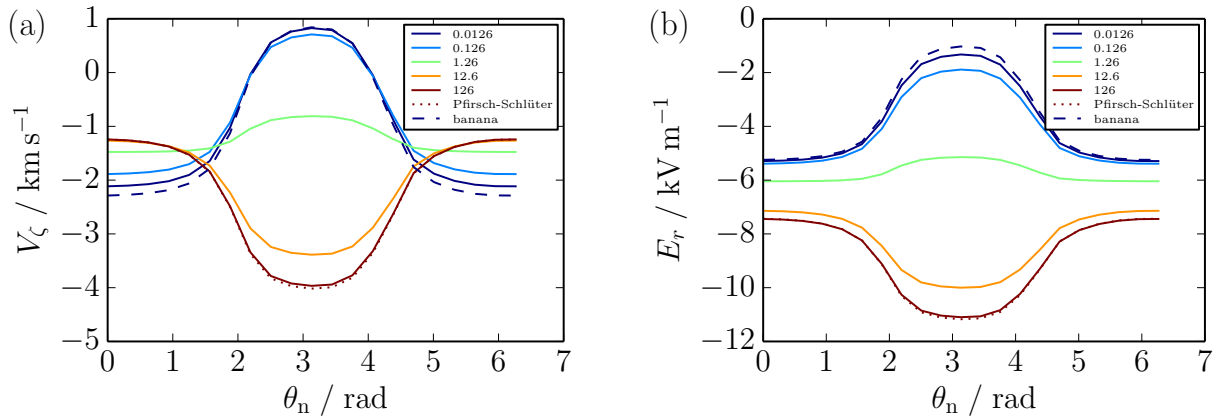
Figure 1. Comparison of analytical and numerical results for the dependence of (a) toroidal flow velocity and (b) radial electric field at the outboard midplane on poloidal location of the neutrals. Dashed lines show the banana regime analytic results, (23) and (22), and dotted lines the Pfirsch-Schlüter analytic results, (20) and (19). Solid lines show numerical scans, with colours from blue to red corresponding to low to high collisionality $\hat{\nu}$, as shown in the legend. A typical ion temperature scale length of 10 cm is taken, to remove the normalizations and give explicit rotation velocity and electric field values. $\theta_{\mathrm{n}} = 0$ is the outboard midplane.

gradient $\partial\Phi_0/\partial\psi$ terms in the drift kinetic equation have identical velocity space structures. Therefore when we solve for $\partial\Phi_0/\partial\psi$ any density gradient gives an offset to $\partial\Phi_0/\partial\psi$ without affecting the flow on the flux surface we consider, as can be seen in Eq. (18).

3.1. Comparison to analytical theory

Analytical forms for the radial electric field and toroidal flow that result from momentum transport by neutrals were calculated in the Pfirsch-Schlüter and banana regimes in Ref. [11]. The electric field $-d\Phi_0/d\psi$ is a flux function, but $V_{\mathrm{i}\zeta}$ varies poloidally and depends on both the major radius where the neutrals are localized, R_{n}, and the major radius where $V_{\mathrm{i}\zeta}$ is evaluated, R. In the Pfirsch-Schlüter regime

$$-\frac{d\Phi_0}{d\psi}(R_{\mathrm{n}}) = \frac{T_{\mathrm{i}}}{en_{\mathrm{i}}}\frac{dn_{\mathrm{i}}}{d\psi} + \frac{1}{e}\frac{dT_{\mathrm{i}}}{d\psi}\left(2 + \frac{(k-1)I^2}{\langle B^2\rangle R_{\mathrm{n}}}\right) \tag{19}$$

$$V_{\mathrm{i}\zeta}(R, R_{\mathrm{n}}) = \frac{I^2}{e\langle B^2\rangle R}\frac{dT_{\mathrm{i}}}{d\psi}\left(\frac{\langle B^2\rangle R^2}{I^2} - \frac{R^2}{R_{\mathrm{n}}^2} + k\left(\frac{R^2}{R_{\mathrm{n}}^2} - 1\right)\right) \tag{20}$$

and the coefficient k is

$$k = 1.97 + 0.09\frac{\langle B^2\rangle\left\langle\left(\nabla_\parallel \ln B\right)^2\right\rangle}{\left\langle\left(\nabla_\parallel B\right)^2\right\rangle}, \tag{21}$$

with the numerical prefactors corrected by a more accurate, numerical solution to the relevant Spitzer problems [34].

In the banana regime,

$$-\frac{d\Phi_0}{d\psi}(R_n) = \frac{T_i}{en_i}\frac{dn_i}{d\psi} + \frac{1}{e}\frac{dT_i}{d\psi}\left(2 + (k-l)\frac{f_2}{f_c}\frac{B_n I^2}{\langle B^2\rangle^{3/2} R_n^2}\right) \tag{22}$$

$$V_{i\zeta}(R,R_n) = \frac{I^2}{e\langle B^2\rangle R}\frac{dT_i}{d\psi}\left(\frac{\langle B^2\rangle R^2}{I^2} - k + (k-l)\frac{f_2}{f_c}\frac{R^2 B_n}{R_n^2 \sqrt{\langle B^2\rangle}}\right), \tag{23}$$

where for a pure plasma

$$k = -1.17/(1 + 0.46 f_t/f_c); \quad l = 1/(1 + 0.46 f_t/f_c), \tag{24}$$

using an interpolation formula [26, 35] between the exact results for large and unit aspect ratio, with the usual definition of the fraction of circulating particles

$$f_c = 1 - f_t = \frac{3}{4}\langle B^2\rangle \int_0^{B_{\max}^{-1}} d\lambda \frac{\lambda}{\langle\sqrt{1-\lambda B}\rangle}; \quad f_2 = \frac{15}{16}\langle B^2\rangle^{3/2} \int_0^{B_{\max}^{-1}} d\lambda \frac{\lambda^2}{\langle\sqrt{1-\lambda B}\rangle}. \tag{25}$$

Fig. 1 shows the simulation results of a scan in the poloidal angle θ_n at which the neutrals are localized in the nominal geometry for a wide range of collisionalities. The analytical limits quoted above are also shown and good agreement can be seen at both high and low collisionality, verifying our numerical implementation. The trends are as expected from the discussion in Sec. 2.2.

3.2. Low order shaping parameters
In Ref. [23] we studied the effect on the electric field and rotation of varying the shaping parameters while keeping the neutrals localized at $\theta_n = \theta_X$, where θ_X is the poloidal angle of the X-point, representing a divertor recycling source or private flux region fuelling. We concluded that the shaping parameters most relevant for machine operation, triangularity and X-point position, only affect the electric field and rotation by changing the major radius where the neutrals are localized, for a fixed collisionality. Here we show that the same is true for the elongation κ, as long as we hold fixed the temperature gradient in poloidal flux space $dT_i/d\psi$ rather than the radial gradient dT_i/dr. Figs. 2(c,d) show that varying κ does not change the radial electric field or rotation, as expected since the major radius of the X-point does not vary with κ.

In contrast the response to varying the inverse aspect ratio ϵ does not follow the same trend with the major radius where the neutrals are localized. In Ref. [23] we found that the electric field increased with R_n at high collisionality and decreased at low collisionality. The radius of the X-point decreases with increasing ϵ, so Fig. 2(b) shows an opposite trend. In the unit aspect ratio limit, the mirror force on the inboard side becomes large and suppresses poloidal flow, so that the contributions parallel to $\boldsymbol{B}$ in (16) and (17) vanish in this limit. This leaves only the rigid rotation parts of the flow and heat flux, which are independent of collisionality. The electric field then approaches $-d\Phi_0/d\psi = (2/e)\,dT_i/d\psi \approx -0.547\,\text{kV T}^{-1}\,\text{m}^{-2}$ (recall that $dn_i/d\psi = 0$ here) and the outboard midplane toroidal rotation approaches $V_{i\zeta} = (R/e)dT_i/d\psi \approx -3.39\,\text{km s}^{-1}$, as can be seen in Figs. 2(a,b). In the large aspect ratio limit $\epsilon \to 0$, $f_t \to 0$ so $l \to 1$ in the banana regime (recall that $l = 1$ generally in the Pfirsch-Schlüter regime) while $\langle B^2\rangle \to I^2/R^2$ so we see from (17) that $q_{i,\zeta} \to 0$. As discussed in section 2.2 the heat flux gives rise to the intrinsic momentum flux that drives rotation, Eq. (15), and so the rotation also vanishes $V_{i\zeta} \to 0$ in this limit.[3]

---

[3] Again, we ought to account for the third Legendre harmonic component as well as the heat flux, but the accurate banana regime result (23) shows that the rotation indeed vanishes, since $f_2 \to 1$ while $R \approx R_n \approx R_0$ and $\sqrt{\langle B^2\rangle} \approx B_n \approx B_0$.
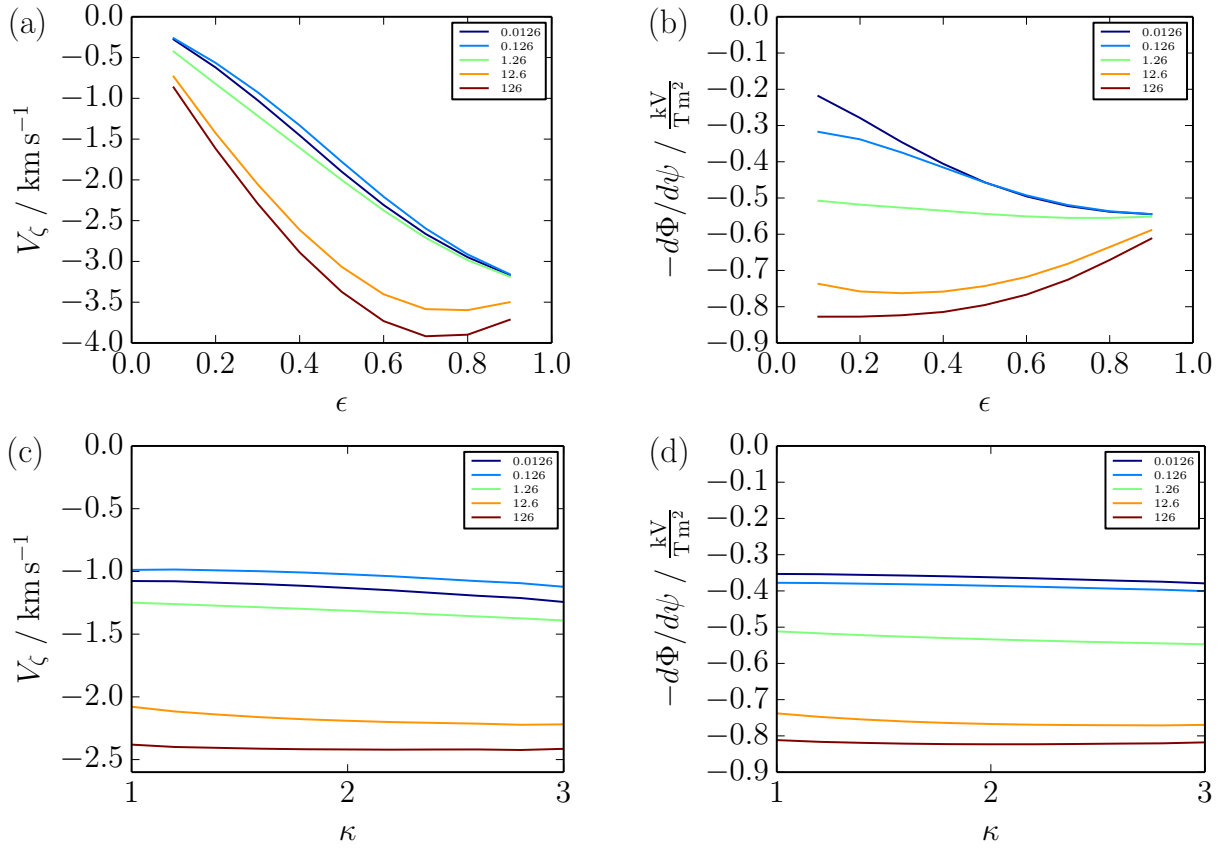
Figure 2. Response of the toroidal rotation $V_{i\zeta}$ and electric field $-d\Phi_0/d\psi$ at the outboard midplane to varying inverse aspect ratio ϵ (a,b) and elongation κ (c,d) for several collisionalities, with neutrals localized at the X-point. The shaping parameters not being scanned are kept at the baseline values. Colours blue to red again correspond to low to high collisionalities as shown in the legend. $dT_i/d\psi$ is held constant at the value corresponding to a gradient length scale of 10 cm in the baseline geometry.

3.3. Impurity rotation

Tokamak rotation is most often measured by charge exchange recombination spectroscopy [24]. Due to the high background of deuterium D_α radiation, an impurity species is most often used for the measurement. However, it is well known both theoretically [25] and experimentally [36] that impurity and bulk ion rotation may differ. For a trace impurity species, we may assume that the presence of the impurity does not affect the momentum transport through neutrals, and by including the impurity in our PERFECT simulations we can calculate the impurity rotation along with that of the main ions, for arbitrary collisionality of either species. The result is shown in Fig. 3(a) for a trace, fully ionized carbon impurity with density $n_z \approx 0.018 n_i$ where the neutrals are localized at the outboard midplane. Ref. [37] gives a convenient form in their Eq. (15) for the velocity difference between bulk ions and a collisional impurity, based on the results of Refs. [25, 38]. Here we neglect all $\mathcal{O}(Z^{-1})$ terms for consistency, where Z is the atomic number of the impurity. These analytical results for collisional and mixed collisionality (banana bulk ion and Pfirsch-Schlüter impurity) limits are compared to the simulation results in Fig. 3(b). The trends agree well, the $\sim 30\%$ discrepancy is consistent with $\mathcal{O}(Z^{-1})$ errors for carbon and the approximate collision operators used analytically. The analytical results show that the velocity difference is independent of the radial electric field, and therefore independent of the location
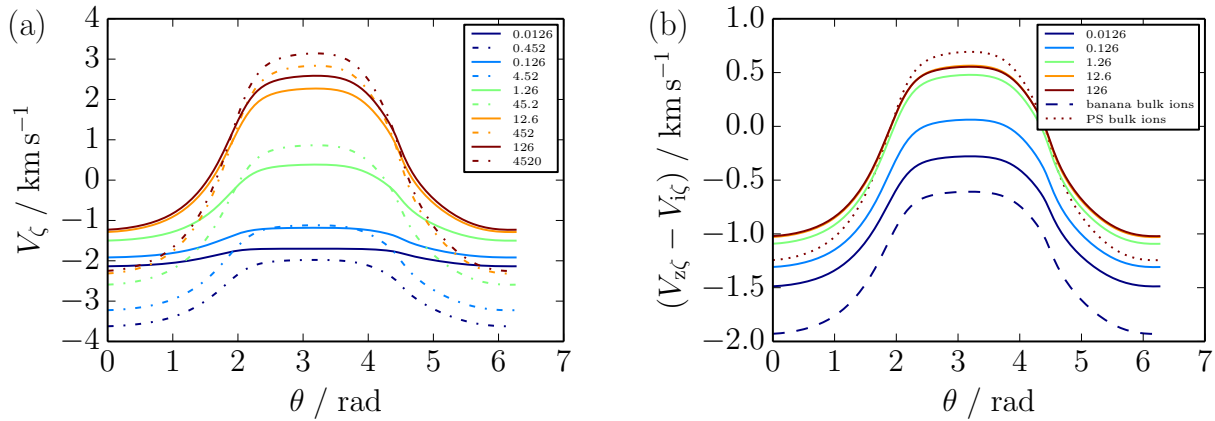
Figure 3. Poloidal variation of (a) the toroidal velocity of bulk ions (solid) and trace, fully ionized carbon impurity (dash-dotted) for neutrals localized at the outboard midplane $\theta_n = 0$ and (b) the difference between carbon and bulk ion velocities (solid), compared to analytical limits with collisional impurity and collisional (dotted) or banana regime (dashed) bulk ions. Colours from blue to red correspond to low to high collisionality $\hat{\nu}$, as shown in the legend. In (b), only the bulk ion collisionality is quoted. The ion temperature scale length is again taken to be 10 cm to produce explicit values. $\theta = 0$ is the outboard midplane.

of the neutrals in our framework, and indeed Fig. 3(b) is identical for simulations with different neutral locations. The quantitative differences highlight the importance of accurate numerical results for the interpretation of experimental impurity rotation measurements.

4. Conclusions

By considering the transport of toroidal momentum through charge-exchanging neutrals, we calculate the radial electric field and intrinsic rotation in a tokamak without external torque, where the flows are subsonic. We have compared the results of our numerical framework first presented in Ref. [23] to the analytical limits of Ref. [11] (with more accurate collisional flow coefficients) finding good agreement in both collisional and collisionless limits. We have extended the investigation of Ref. [23] to lower order shaping parameters, finding that the elongation κ has little effect on the electric field and rotation due to neutrals. In contrast, varying the inverse aspect ratio ϵ has more fundamental effects, for instance changing the mirror forces, resulting in trends in electric field and rotation that are not captured just by the collisionality and the major radius where the neutrals are localized, R_n. Finally, in order to facilitate comparisons to experimental measurements which usually obtain impurity rotation by charge exchange recombination spectroscopy, we have demonstrated that impurities can be included in the framework. Here we neglect their interactions with the neutrals, so impurities may be present only in trace quantities, but arbitrary collisionality of either ion species can be treated.

References
[1] Hender T *et al.* 2007 *Nucl. Fusion* **47** S128

[2] Terry P W 2000 *Rev. Mod. Phys.* **72**(1) 109

[3] Hazeltine R, Calvin M, Valanju P and Solano E 1992 *Nucl. Fusion* **32** 3

[4] Catto P J 1994 *Phys. Plasmas* **1** 1936

[5] Helander P, Krasheninnikov S I and Catto P J 1994 *Phys. Plasmas* **1** 3174

[6] Catto P J *et al.* 1998 *Phys. Plasmas* **5** 3961

[7] Fülöp T *et al.* 1998 *Phys. Plasmas* **5** 3398

[8] Fülöp T *et al.* 1998 *Phys. Plasmas* **5** 3969

[9] Fülöp T *et al.* 2001 *Phys. Plasmas* **8** 5214

[10] Fülöp T *et al.* 2002 *Phys. Rev. Lett.* **89**(22) 225003

[11] Helander P *et al.* 2003 *Phys. Plasmas* **10** 4396

[12] Carreras B A *et al.* 1998 *Phys. Plasmas* **5** 2623

[13] Owen L W *et al.* 1998 *Plasma Phys. Controlled Fusion* **40** 717

[14] Gohil P *et al.* 2001 *Phys. Rev. Lett.* **86**(4) 644

[15] Boivin R L *et al.* 2000 *Phys. Plasmas* **7** 1919

[16] Field A R *et al.* 2002 *Plasma Phys. Controlled Fusion* **44** A113

[17] Valovic M *et al.* 2002 *Plasma Phys. Controlled Fusion* **44** A175

[18] Fukuda T *et al.* 2000 *Plasma Phys. Controlled Fusion* **42** A289

[19] Field A R *et al.* 2004 *Plasma Phys. Controlled Fusion* **46** 981

[20] Maingi R *et al.* 2004 *Plasma Phys. Controlled Fusion* **46** A305

[21] Joffrin E *et al.* 2014 *25th IAEA Fusion Energy Conference (FEC 2014)* EX/P5-40

[22] Tamain P *et al.* 2015 *J. Nucl. Mater.* **463** 450

[23] Omotani J *et al.* 2016 *Nuclear Fusion* **56** 124002

[24] Isler R C 1994 *Plasma Phys. Controlled Fusion* **36** 171

[25] Kim Y B, Diamond P H and Groebner R J 1991 *Phys. Fluids B* **3** 2050

[26] Helander P and Sigmar D J 2002 *Collisional transport in magnetized plasmas*

[27] Rosenbluth M N *et al.* 1971 *Plasma Phys. Controlled Nucl. Fusion Res., Volume I* p 495

[28] Hazeltine R D 1974 *Phys. Fluids* **17** 961

[29] Catto P J and Simakov A N 2005 *Phys. Plasmas* **12** 012501

[30] Helander P 1999 *Proceedings of the Joint Varenna-Lausanne Workshop* ed Connor J W, Sindoni E and Vaclavik J (Bologna) p 373

[31] Summers H P 2004 *The ADAS User Manual, v. 2.6* (http://www.adas.ac.uk)

[32] Landreman M *et al.* 2014 *Plasma Phys. Controlled Fusion* **56** 045005

[33] Cerfon A J and Freidberg J P 2010 *Phys. Plasmas* **17** 032502

[34] Landreman M 2013 *private communication*

[35] Taguchi M 1988 *Plasma Phys. Controlled Fusion* **30** 1897

[36] Kim J *et al.* 1994 *Phys. Rev. Lett.* **72**(14) 2199

[37] Catto P J and Simakov A N 2006 *Phys. Plasmas* **13** 052507

[38] Hirshman S and Sigmar D 1981 *Nucl. Fusion* **21** 1079